PCCP

Accepted Manuscript

ROYAL SOCIETY OF CHEMISTRY

www.rsc.org/pccp

Journal Name

ARTICLE

Quantum Trajectory Monte Carlo Method for Study of Electron-Crystal Interaction in STEM

Z. Ruan,[a] R.G. Zeng,[b] Y. Ming,[c,†] M. Zhang,[a] B. Da,[a] S.F. Mao,[d] and Z.J. Ding[a,*]

Received 00th January 20xx,
Accepted 00th January 20xx

DOI: 10.1039/x0xx00000x

www.rsc.org/

In this paper, a novel quantum trajectory Monte Carlo simulation method is developed to study electron beam interaction with a crystalline solid for application to electron microscopy and spectroscopy. The method combines the Bohmian quantum trajectory method, which treats electron elastic scattering and diffraction in a crystal, with a Monte Carlo sampling of electron inelastic scattering events along quantum trajectory paths. We study in this work the electron scattering and secondary electron generation process in crystals for a focused incident electron beam, leading to understanding of the imaging mechanism behind the atomic resolution secondary electron image that has been recently achieved in experiment with a scanning transmission electron microscope. By the method the Bohmian quantum trajectories have been calculated at first through a wave function which is obtained by a numerical solution of the time-dependent Schrodinger equation with a multislice method. The impact parameter dependent inner-shell excitation cross section then enables the Monte Carlo sampling of ionization events produced by incident electron trajectories travelling along atom columns for excitation of high energy knock-on secondary electrons. Following cascade production, transportation and emission processes of true secondary electrons of very low energies is traced by a conventional Monte Carlo simulation method to present image signals. Comparison of the simulated image for a Si (110) crystal with the experimental image indicates that dominant mechanism of atomic resolution of secondary electron image is the inner-shell ionization events generated by a high energy electron beam.

Introduction

With the development of probe-aberration correction technology the electron probe size has been reduced to less than 1 Å. The fine probe size enables atomic resolution for many probe-based imaging modes, such as, annular dark field imaging and electron energy loss spectroscopy imaging, in a scanning transmission electron microscope (STEM).[1,2] It has been reported only recently that an atomic resolution secondary electron (SE) image can be obtained in an aberration corrected STEM equipped with an SE detector above specimen.[3,4] These breakthroughs in resolution open new views of materials[5]; it is thus extremely important to study the electron-solid interaction at atomic scale in very details for quantitative interpretation of electron microscopic image and energy spectra in experiments.

The theory of electron-solid interaction is a vital fundament for many material analysis techniques, such as electron spectroscopy, diffraction and microscopy. The present computational methods for study of electron-solid interaction can be divided into two categories, i.e. classical and quantum mechanical. The conventional Monte Carlo simulation of classical electron trajectories has been proven a powerful tool for study of electron-solid interaction and SE generation in amorphous solids.[6-8] However, this classical modeling cannot take the crystal structure information into account, resulting in neglect of the electron coherent scattering, which is indispensable in electron interaction with crystal. On the other hand, quantum mechanical methods based on wave nature description of particle, such as Bloch wave method[9] and multislice method[10], show great success in studying diffraction effects[11]. Unfortunately, considering the complexity of calculation, it seems too difficult to include the electron inelastic scattering and associated SE cascade process in these quantum mechanical methods. Meantime, the particle trajectory character with probability wave motion behavior has been clearly demonstrated in the single electron buildup of an interference pattern experiment[12]. Although the classical noncoherent and quantum mechanical methods have their own applicable scopes, but a comprehensive theoretical investigation of electron interaction with crystalline solid is required to be able to represent the wave-particle duality nature of microscopic particle. Such a theoretical frame can then offer a physical picture of diffraction in terms of the established classical trajectory picture intuitively.

This work aims to develop a new quantum trajectory Monte Carlo (QTMC) method to study electron interaction with

[a] Hefei National Laboratory for Physical Sciences at Microscale and Department of Physics, University of Science and Technology of China, Hefei, Anhui 230026, P.R. China
[b] Science and Technology on Surface Physics and Chemistry Laboratory, P.O. Box 718-35, Mianyang, Sichuan 621907, P.R. China
[c] School of Physics and Material Science, Anhui University, Hefei, Anhui 230601, P.R. China
[d] School of Nuclear Science and Technology, University of Science and Technology of China, Hefei, Anhui 230026, P.R. China
† E-mail: meanyee@mail.ustc.edu.cn
* E-mail: zjding@ustc.edu.cn

crystalline solid by combining a quantum trajectory method for treating electron elastic scattering and diffraction with a conventional Monte Carlo sampling of electron inelastic scattering events along quantum trajectory path. The quantum trajectory method, which was developed by de Broglie[13] and Bohm[14,15], can not only interpret quantum phenomena accurately as in standard quantum mechanics, but also has the ability to provide an intuitive physical picture based on classical particle trajectory picture[16]; therefore, it is suitable to formulate a QTMC scheme for electron trajectory calculation. The theory postulates coexistence of quantum wave and particles with the particle position distribution governed by the modulus squared of the wave function. The particle position and momentum can be simultaneously determined from solution of quantum Hamilton-Jacobi (HJ) equation. This quantum trajectory theory has been successfully used to study many quantum phenomena, such as tunneling mechanism[17], two-slit diffraction experiment[18], intense laser-atom physics[19] and electron diffraction in crystal[20]. By QTMC method the quantum trajectories represent in nature the moving directional change of electrons in elastic scattering with lattice atoms during their propagation; in addition, electron inelastic scattering and cascade SE's production and transportation processes have been integrated through a conventional Monte Carlo sampling procedure. Considering the fact that SEs contributing to the localized image signals should be initially generated from inner-shell ionization events[21], then we have introduced impact-parameter dependent ionization cross-section to simulate high energy knock-on SEs excitation. The hydrogenic model[22] is used to describe the inner-shell excitation based on wave mechanics for the hydrogen atom. The successive cascade production of low energy SE signals, which may destroy the local image information at atomic scale, can be treated with a conventional Monte Carlo simulation method.[6]

In this paper, firstly we have studied the wave function propagation and the quantum trajectories in a Cu crystal for a convergence coherent electron probe. An intuitive interpretation of the electron diffraction process in Cu crystal has been performed by the obtained quantum trajectories. Then simulation of atomic resolution SE imaging has been performed for atom columns in a Si (110) crystal and compared with an experiment. Many efforts have been put into exploration of mechanism for atomic resolution SE imaging.[4,23,24] Inner-shell ionization for high energy SE production was proposed to be the source for the atomic image contrast. However, actually what they considered was the high energy knock-on SEs generated right away from the inner-shell ionization with kinetic energies above hundreds of eV, but not the true low energy SE signals used in practical imaging, whose energies are only several eV as in SEM. Not only the probe size but also the cascade process for production of such low energy SE signals in a much wider spatial region in the interaction range of the order of 100 nm depending on electron energy and target density[25], had been considered to destroy the local information in SE imaging, and, thus the atomic resolution image would not be possible. Therefore, in order to clarify the imaging mechanism the full description of the whole signal generation process should be made by combing the inner-shell excitation of knock-on SEs with cascade production of low energy SEs. For this, the present QTMC modeling includes every experimental and physical factor in SE generation, transportation and emission in a crystalline solid. The quantum trajectories of primary electrons in a Si crystal are calculated for a 200-keV coherent convergence electron beam; the atomic resolution SE image of Si (110) lattice has been obtained and compared with an experimental image, which shows the Si dumbbells at spacing of 1.4 Å.[4,26]

Quantum Trajectory Monte Carlo method

In our QTMC method, elastic scattering and diffraction events for incident electrons are treated by Bohmian quantum trajectory method, and, the inelastic scattering events along quantum trajectory path are simulated by a conventional Monte Carlo sampling technique. The modeling of SE image signal forming process by the QTMC method is schematically displayed in Fig. 1(a). In this scheme the simulation of atomic resolution SE imaging is composed of two steps: The first step deals with the high energy SE excitation in inner-shell ionization events by the inelastic interaction of the fast incident electrons with crystalline atoms, while the elastic interaction process involving diffraction of incident electrons is treated by the Bohmian quantum trajectory method. High energy SEs are generated according to the cross section of inner-shell ionization, which is dependent of the position of an moving electron at its trajectory path. The second step handles the cascade production and emission of low energy SEs by the decay of high energy knock-on SEs; this SE diffuse and emission process is studied with a conventional Monte Carlo method for amorphous solid as schmatically shown in Fig. 1(b).

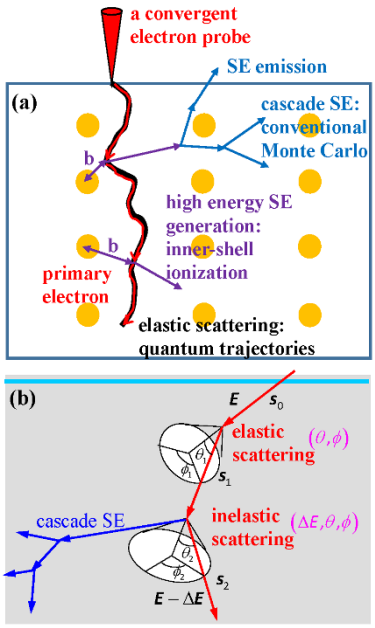

Fig. 1 The illustration of quantum trajectory Monte Carlo (QTMC) method. (a) The SE image signal forming process in crystalline specimen; (b) the conventional Monte Carlo sampling for the SE transportation and cascade process.

Quantum trajectory

According to the Bohmian quantum trajectory theory[14,15], the wave function represents an objectively real field associated with a set of trajectories of particles. Rewritting the wave function $\psi(\mathbf{r},t)$ in the time-dependent Schrödinger equation (TDSE), $i\hbar\partial\psi(\mathbf{r},t)/\partial t=\left(-\hbar^2\nabla^2/2m+V\right)\psi(\mathbf{r},t)$, where V is the external potential, in a polar form $\psi(\mathbf{r},t)=R(\mathbf{r},t)\exp\left(iS(\mathbf{r},t)/\hbar\right)$, where R and S are real functions representing respectively the amplitude and phase of wave function, the TDSE is separated into real and imaginary parts; the two associated equations are then obtained as,

$$-\frac{\partial S}{\partial t}=\frac{(\nabla S)^2}{2m}+V-\frac{\hbar^2}{2m}\frac{\nabla^2 R}{R}, \quad (1)$$

$$\frac{\partial R^2}{\partial t}+\nabla\left(\frac{R^2\nabla S}{m}\right)=0. \quad (2)$$

where $\hbar$ is the Planck constant and m the particle mass. Eq. (1) is referred to quantum Hamilton-Jacobi (HJ) equation, which differs from the classical HJ equation by only an additional quantum potential term, $-\hbar^2\nabla^2R/2mR$, due to internal quantum forces. As in the classical HJ theory, the velocity field for Bohmian particle is defined as,

$$\mathbf{v}=\frac{\nabla S(\mathbf{r},t)}{m}=\frac{\hbar}{m}\mathrm{Im}\frac{\nabla\psi(\mathbf{r},t)}{\psi(\mathbf{r},t)}. \quad (3)$$

Then the quantum trajectory of the Bohmian particle associated to a given quantum state can be calculated by integrating the velocity field as,

$$\mathbf{r}(t)=\mathbf{r}_0(t_0)+\int_{t_0}^{t}(\nabla S/m)dt. \quad (4)$$

The methods for calculating the quantum trajectories are classified into two catagories. One is to obtain S by directly solving Eqs. (1) and (2). The second-order derivatives of R and S have to be calculated by these methods, which is quite difficult at present.[27] The other one firstly derives the wave function by solving the TDSE and the velocity field is then obtained from wave function by Eq. (3). Because there are many robust methods developed to solve the TDSE, such as split operator method[28], multislice method[29], Bloch wave method[30], the later catagory of methods is easier and more efficient in simulation. In this study, we employ the multislice method, which is popular used in studying wave function propagation in crystal, to solve the TDSE and then calculate the quantum trajectories from the obtained wave function.

To solve the TDSE in crystal, the crystalline potential for electron scattering inside a crystal should be firstly given. For most of inorganic crystals, the crystalline potential can be approximated as the superposition of electrostatic potential of single neutral atoms[31],

$$V(\mathbf{r})=\sum_n\sum_i\phi_i(\mathbf{r}-\mathbf{R}_n-\mathbf{r}_i), \quad (5)$$

where $\mathbf{R}_n$ represents the coordinate of nth unit cell, and $\mathbf{r}_i$ the coordinate of ith atom in the unit cell. The electrostatic potential of a single isolated atom, $\phi(\mathbf{r})$, can be obtained via inverse Fourier transform of the atomic scattering factor.[32]

The multislice approach can be used for studying the electron scattering in crystal for a convergence coherent probe. The initial wave function can be described as a coherent sum of plane waves, each having an appropriate phase relationship[33],

$$\psi_p(\mathbf{r}-\mathbf{r}_0)=\int A(\mathbf{k}_\parallel)\exp(i\chi)\exp\left[2\pi i\mathbf{k}_\parallel\cdot(\mathbf{r}-\mathbf{r}_0)+2\pi ik_z z\right]d\mathbf{k}_\parallel, \quad (6)$$

where $A(\mathbf{k}_\parallel)$ is the aperture function, $\mathbf{r}_0$ the center of the beam probe, $\mathbf{k}_\parallel$ the transverse component of each plane wave having a wave length of λ, and χ describes the phase change due to the probe-forming lens.[34]

Here, single-electron approximation is applied in the present QTMC method, which is used for study of the electron-crystal interaction in STEM, in which the incident electron energy is such high, usually hundreds of keV, that exchange interaction can be ignored[35]. However, this method can also be improved to include the electron correlation. There are several studies on a many-particle quantum system by using the quantum trajectory method, taking account of correlation interaction among electrons[36,37].

Inner-shell and valence excitations

Besides elastic scattering along the quantum trajectory paths, the incident electrons can also transfer energy to atoms in the crystal if their trajectories are close enough to the atoms, and, result in inner-shell excitation events. High energy knock-on SEs generated in inner-shell excitation events, which are considered as primary source of atomic scale SE imaging, are taking into account in present QTMC modeling by sampling along the quantum trajectory paths whenever the cross-section of inner-shell ionization is given.

The hydrogenic model[22] is utilized to present the impact parameter dependent inner-shell ionization cross-section via generalized oscillator strength (GOS). The double differential inelastic cross-section for inner-shell ionization per atom is given in the first Born approximation as[38],

$$\frac{d^2\sigma}{d\Omega d(\Delta E)}=\frac{e^4}{E\Delta E\left(\theta^2+\theta_E^2\right)}\frac{df(q,\omega)}{d(\Delta E)}, \quad (7)$$

where θ is scattering angle, $d\Omega=2\pi\sin\theta d\theta$ the solid angle interval, e the electron charge, $E=\hbar^2k^2/2m$ the kinetic energy of a moving electron, $\Delta E=\hbar\omega$ the energy loss, $\theta_E=\hbar\omega/2E$, and $\hbar q=\hbar k\sqrt{\theta^2+\theta_E^2}$ the momentum transfer. $df(q,\omega)/d(\Delta E)$ represents the GOS, describing the response of an atom for a given energy- and momentum-transfer from an external source. The impact parameter b can be estimated from the uncertainty principle, $\Delta x\Delta p\sim\hbar$, where Δx equals to the impact parameter b and $\Delta p=\hbar q$ is the momentum transfer. Rewriting Eq. (7) in impact parameter representation gives[39],

$$\frac{d^2\sigma}{dbd(\Delta E)}=\frac{e^4}{E\Delta E}\frac{1}{b}\frac{df}{d(\Delta E)}. \quad (8)$$

To obtain the ionization cross-section, the impact parameter dependent GOS should be calculated firstly. The simplest way to estimate GOS is based on a hydrogenic model by solving the Schrodinger equation,

$$\left(-\hbar^2/2m\right)\nabla^2\psi-\left(Z_s e^2/4\pi\varepsilon_0 r\right)\psi+E_s\psi=E_t\psi, \quad (9)$$

where ε_0 is the vacuum dielectric constant. For K-shell, as an example, $E_t=\Delta E-E_K$ is the kinetic energy of the knock-on K-shell electron, relating to the orbital binding energy E_K and the acquired loss energy ΔE from the incident electron. An

effective nuclear charge $Z_s e$ is used to describe a reduction of nuclear charge by 1*s* electron as, $Z_s = Z - 0.3$. Outer electrons are assumed to form a spherical shell of charge, reducing the inner-shell binding energy by an amount of E_s, so that the observed binding energy is $E_K = Z_s^2 R - E_s$ [22,40], where $R = 13.6$ eV is the Rydberg energy.

Defining two dimensionless quantities, $k_H^2 = \Delta E / Z_s^2 R - 1$ and $Q' = \left(q a_0 / Z_s\right)^2$, then the GOS of *K*-shell electrons is given as[40],

$$\frac{df_K}{d(\Delta E)} = \frac{256\Delta E\left(Q' + k_H^2/3 + 1/3\right)}{Z_s^4 R^2\left[\left(Q' - k_H^2 + 1\right)^2 + 4k_H^2\right]^3} \times \begin{cases} \dfrac{\exp\left(-2\beta'/k_H\right)}{\left[1 - \exp\left(-2\pi/k_H\right)\right]}, & k_H^2 > 0; \\ \exp(y), & k_H^2 < 0. \end{cases} \tag{10}$$

In the above formula, for $k_H^2 > 0$, $\beta' = \arctan\left[2k_H / \left(Q' - k_H^2 + 1\right)\right]$; for $k_H^2 < 0$, $y = -\ln\left[\left(Q' + 1 - k_H^2 + 2|k_H|\right) / \left(Q' + 1 - k_H^2 - 2|k_H|\right)\right] / |k_H|$. The corresponding hydrogenic formulas have also been derived for *L*-shell[41,42] and *M*-shell[43]. For *L*- and *M*-shells, we have used formulas based on a modified hydrogenic model by adding an empirical correction factor from the photon absorption data.[44]

Egerton et al.[22] have calculated *K*-shell photoabsorption cross-section for several elements by a hydrogenic model and compared with experimental data and Hartree-Slater calculations; the results reveal that the hydrogenic model is effective for description of inner-shell ionization. In the following simulation of atomic resolution SE imaging for Si (110) lattice, we have included electron excitations from *K*- and *L*-shells. Fig. 2(a) shows the total ionization cross-sections, σ, of Si for *K*-, L_1- and $L_{2,3}$-shells calculated by the hydrogenic model, i.e. by integrating Eq. (8), where the ionization energies for *K*-, L_1- and $L_{2,3}$-shells of Si are, respectively, 1839.0, 149.7 and 99.5 eV. They are found in good agreement with Casnati's ionization cross-section[45], which has been regarded as the best empirical formula for inner-shell ionization cross-section. The impact parameter dependent differential inner-shell ionization cross-sections calculated for electron energy of 200 keV are shown in Fig. 2(b). By the hydrogenic model there is a maximum ionization probability when the impact parameter *b* is about subangstrom distance away from an atomic nucleus. The inner-shell ionization probability firstly increases with the impact parameter and then decreases, indicating that the inner-shell electrons are likely to be excited when the incident electrons moving closer enough to the atoms.

In addition to inner-shell ionization, electrons also suffer inelastic scattering due to valence electron excitation in a solid with much higher probability but in much lower energy loss. In a dielectric functional approach the overall differential cross-section for electron inelastic scattering is given as,

$$\frac{d^2\lambda_{in}^{-1}}{d\omega dq} = \frac{\hbar}{\pi a_0 E}\mathrm{Im}\left\{\frac{-1}{\varepsilon(q,\omega)}\right\}\frac{1}{q}, \tag{11}$$

where a_0 is the Bohr radius, $\hbar\omega$ and $\hbar q$ are the energy loss and momentum transfer from an electron with kinetic energy E penetrating into a solid. $\mathrm{Im}\left\{-1/\varepsilon(q,\omega)\right\}$ and $\varepsilon(q,\omega)$ are respectively the energy loss function and the dielectric function of solid. λ_{in} is the electron inelastic mean free path calculated by integration of Eq. (11). For calculating energy loss function,

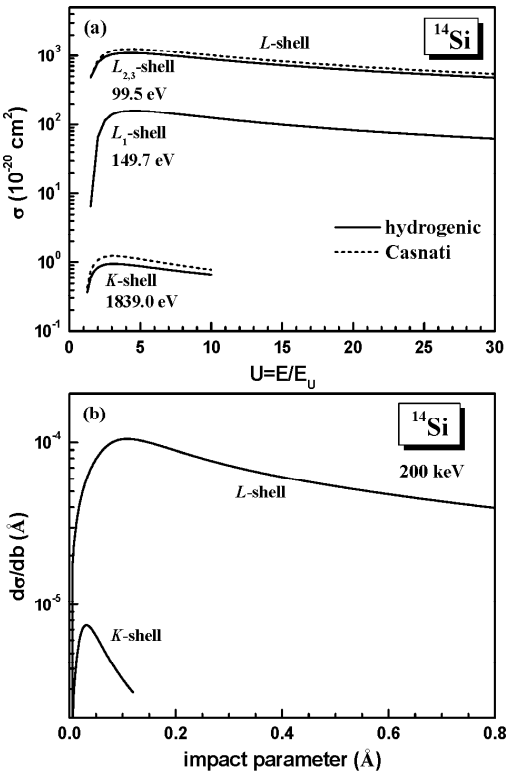

Fig. 2 (a) The ionization cross-sections of Si for *K*- and L_1- and L_{23}-shells calculated by the hydrogenic model (solid lines). The corresponding Casnati cross-sections[45] for *K*- and total *L*-shells (dashed lines) are shown for a comparison; (b) The impact parameter dependent differential inner-shell ionization cross-sections of Si *K*- and total *L*-shells under electron energy of 200 keV.

Penn's extrapolation scheme[46] is applied, using the optical data compiled in a database[47]. More details are described elsewhere.[6-8]

The simulation procedure for the generation of SEs from inner-shell excitation in the QTMC model is illustrated in Fig. 1(a). An incident electron travels along a quantum trajectory made of electron elastic scattering with atom lattice; once it passes by a step length, $s = -\lambda_{\mathrm{in}} \ln R_1$, where $R_1 \in [0,1]$ is a uniform random number, an inelastic scattering event happens. The type of inelastic event, either inner-shell ionization or valence electron excitation, is sampled by the respective cross-sections. The impact parameter dependent total ionization cross-sections of *K*- and *L*-shells through integration of Eq. (8), namely σ_K, σ_{L_1} and $\sigma_{L_{2,3}}$, are used to determine inner-shell excitation channel: if $R_2 < \sigma_K \lambda_{\mathrm{in}}$, where R_2 is another random number, then one *K*-shell electron is excited; similarly, one L_1-shell or $L_{2,3}$-shell electron is excited if $\sigma_K \lambda_{\mathrm{in}} < R_2 < \left(\sigma_K + \sigma_{L_1}\right)\lambda_{\mathrm{in}}$ or $\left(\sigma_K + \sigma_{L_1}\right)\lambda_{\mathrm{in}} < R_2 < \left(\sigma_K + \sigma_{L_1} + \sigma_{L_{2,3}}\right)\lambda_{\mathrm{in}}$ is satisfied respectively. Otherwise, when $R_2 > \left(\sigma_K + \sigma_{L_1} + \sigma_{L_{2,3}}\right)\lambda_{\mathrm{in}}$, it is the valence electron excitation. For inner-shell excitation, the impact parameter is obtained as the distance between the position of the electron on the quantum trajectory and its nearest atom in crystal, shown as *b* in Fig. 1(a). Other distant atoms can be neglected due to the rapid decreasing behavior of ionization cross-section with impact parameter shown in Fig. 2(b). The

energy loss ΔE of the primary electron is decided by sampling from the differential cross-section of Eq. (8) at the given impact parameter *b*. The initial energy of the excited knock-on SE is $E_1 = \Delta E - E_{K,L}$ and the initial moving direction is sampled spatially uniform. For valence excitation, however, Eq. (11) is used instead to sample the energy loss and hence the energy of generated SE.[6] It should be noted that the experimental optical data used in the dielectric functional approach includes also the contribution from inner-shell ionizations; we have to remove the inner-shell edges from experimental optical energy loss function[48] to avoid double counting of the ionizations.

Since the energy loss ΔE is comparatively small with respect to electron energy E, the electron having suffered an inelastic scattering and at an energy of $E - \Delta E$ is treated here to move along the same quantum trajectory as at E in order to avoid the computational complexity. The primary electron continues traveling along the quantum trajectory to enough large depth and the information of all the excited SEs in the path is recorded; these SEs are traced to go on the cascade SE multiplication process by conventional Monte Carlo simulation later.

Cascade SE generation

As schematically illustrated by Fig. 1(a), the position dependent excitation probability enables the high energy knock-on SEs generated in inner-shell ionization events to have their local birth information embodied in the amount of knock-on SEs as a dependence of the scanning position of incident beam. The high energy SEs further transport in the crystal and produce a large number of low energy cascade SE signals for imaging. In this work, we have simulated this multiplication process of SE signal production by a conventional Monte Carlo method, which has been proved to be valid for SE study in previous works for amorphous solids.[6-8] In this classical Monte Carlo simulation, the electron-solid interaction process is described by a series of discrete and randomly sampled elastic and inelastic scattering events, as schematically shown by Fig. 1(b), by neglecting the interference effect of electrons in a crystal which is considered to be negligible due to long wavelengths for very low energy SEs. By this modeling, as a result of an electron inelastic scattering event a loss energy is transferred from the moving electron to a solid and to excite a low energy electron. A cascade production of SEs continue until they either emit from surface or absorbed in the sample by losing entire kinetic energy. Mott's cross section[49] and dielectric functional approach[46] are used to describe the electron elastic scattering and inelastic scattering, respectively.

Results and Discussion

Bohmian quantum trajectories

Quantum trajectory method has been applied to study the channeling effect on electron diffraction in crystalline solid, when a plane wave probe is used[50]. In this work we will study electron-crystal interaction in STEM, hence a convergence coherent probe is used, as defined in Eq. (6). Firstly we have calculated quantum trajectories for electron elastic scattering in Cu crystals for a convergence coherent probe at 100 keV. The crystal potential of Cu single crystal with a lattice constant of 0.36 nm is constructed from the complex atomic scattering factors by Eq. (5). The electron wave function is computed by solving TDSE via multislice method and the Bohmian quantum trajectories are calculated by integrating the velocity field as Eqs. (3) and (4), based on the obtained wave function.

Fig. 3(a) shows several three-dimensional (3D) quantum trajectories in a Cu crystal for a convergent and coherent electron probe as described by Eq. (6). 17 representative electron probe landing sites at the specimen surface are selected for illustration, as shown by the red points in Fig. 3(b). Different propagation behaviors of electron beams landing at different positions have shown that the interaction between electrons and atom column modulates electron trajectories in such a way that the beam tends to move along atom columns. The similar calculation is performed for a Si crystal, shown by Fig. 4, for the subsequent simulation of atomic resolution SE imaging. For better visibility, we only demonstrate quantum trajectories at 13 representative electron probe landing sites,

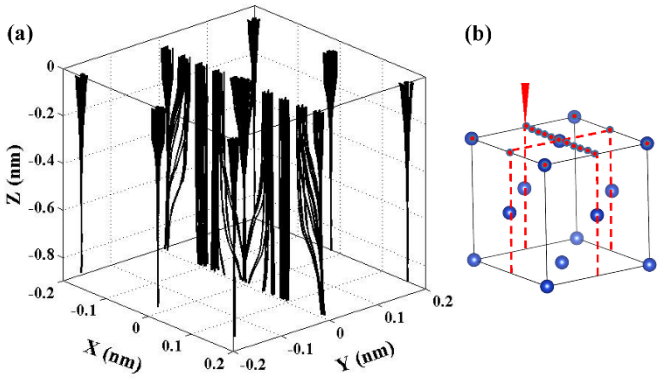

Fig. 3 (a) 3D quantum trajectories in a Cu crystal for a convergent and coherent electron probe of 100 keV incident on the crystal surface at representative landing sites. It is shown 25 quantum trajectories in every electron probe; (b) schematic diagram of 17 selected electron probe landing sites at the specimen surface indicated by red points.

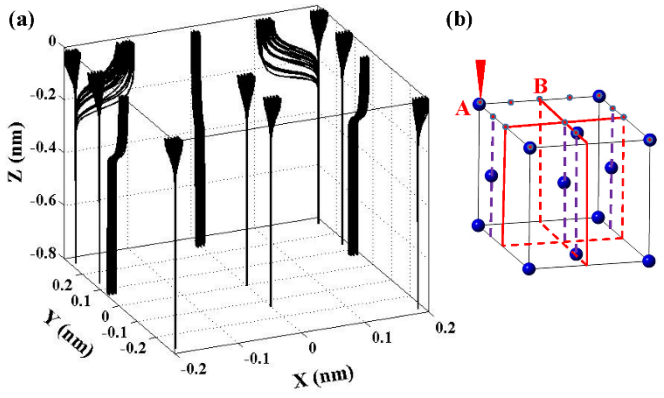

Fig. 4 (a) Several 3D quantum trajectories in Si (110) crystal for a convergent and coherent electron probe of 200 keV incident on the crystal surface at representative landing sites. It is shown 25 quantum trajectories in every electron probe; (b) schematic diagram of 13 selected electron probe landing sites at the specimen surface indicated by red points.

shown as the red points in Fig. 4(b). One can find that, when a focused electron beam is incident near to an atom column, most of electrons become being confined at the column center; while the electron probes landing between two neighboring atom columns will change their moving direction gradually by the attraction of second layer atoms, leading to position dependent image contrast production from inner-shell ionization probability. In addition, there are some differences found between quantum trajectories in Cu and Si crystals: the quantum trajectories are focused along an atom column more quickly in Si crystal than in Cu. For Cu, quantum trajectories incident near to an atom column are focused well at a depth of about 0.4 nm, but for Si it is reduced to less than 0.2 nm. For the beam incoming between atom columns the quantum trajectories are likely bent to the atom positions nearby during the movement of electrons. Clearly, such distinct trajectory behavior comes from the difference of crystalline potentials of two specimen, which are made of atomic potential according to crystalline structure as by Eq. (5); the magnitude and form of a crystalline potential dominate electron elastic scattering and diffraction in a crystal.

In order to see this more clearly, Fig. 5(a) presents two-dimensional (2D) quantum trajectories in a Cu crystal in a cross sectional plane; the Cu crystal potential in the corresponding area is displayed in Fig. 5(b). The quantum trajectories in Fig. 5(a) can be divided into three groups according to their propagation characters in crystal. When the probe is landing at or quite near to an atom column, the incident probe is quickly contracted by the atom column to move along its center, forming a central propagation channel. In such a short distance of the impact parameter between electron trajectory and atomic nucleus, incident beam has rather high inner-shell ionization probability and high energy SEs are likely to be generated. In another group, the incident electrons land just between two atom columns, e.g. $x = 0.09$ nm, the beam propagates almost straightly without changing its moving direction and hence the probe size, forming another propagation channel, the mid channel. Because the electrons transport in this mid channel will locate in a much farther distance to atoms than in the central channel the inner-shell ionization is thus much less probable, considering the rapid decreasing behavior of ionization cross section with increase of impact parameter as shown by Fig. 2(b), particularly for *K*-shell. The third group of electrons land between those of above two groups; the corresponding quantum trajectories then gradually come close to the atom columns after they travel a period of distance inside the crystal; therefore, they can excite high energy SEs at deeper depth under the surface than the first group and the corresponding intensity of SE emission should be smaller considering the exponential decay behavior of SE emission with depth. Fig. 5(c) illustrates the quantum trajectory behavior in a deeper depth region. Electron probe trajectories in the central channel will gradually deviate from the atom column axis after passing through a distance due to the slight convergence angle, and the mid channel will be finally attracted by an atom column. After all, the incident electron beam in a convergent probe form will travel different paths inside the crystal according to its landing position; the distance between

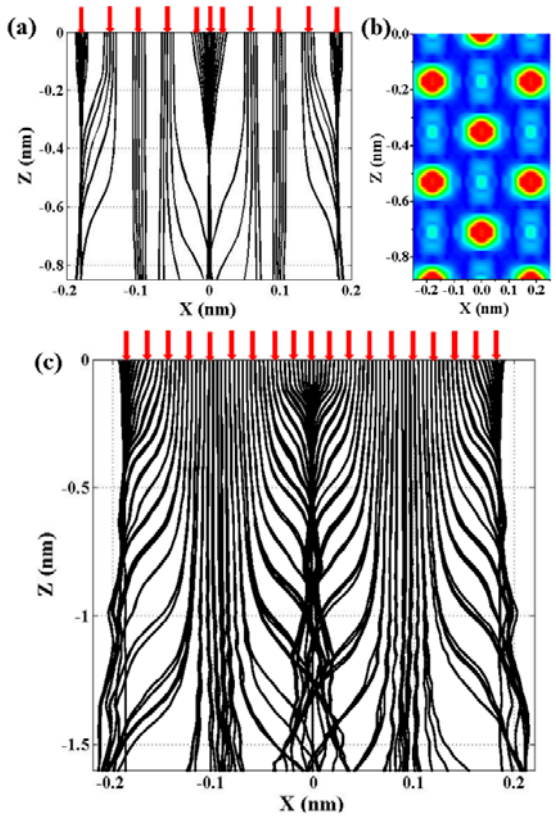

Fig. 5 (a) 2D quantum trajectories of Fig. 3(a) in the *x*-*z* vertical cross sectional plane, where the red arrow indicates the incident location of a convergent electron beam. (b) corresponding intensity map of Cu crystal potential in the same plane as (a); (c) quantum trajectories in an enlarged depth region for an electron probe of 100 keV scanning across *x*-axis with step of 0.02 nm between (-0.18, 0.18) nm. It is shown 25 quantum trajectories in every electron probe.

the quantum trajectories and the crystal atoms will hence affect the ionization cross-section of localized inner-shell electrons. Obviously, the landing position on top surface atoms allows the strongest SE generation and emission, while the position at second layer atoms enables also strong SE generation but not emission. Then the image contrast should depend on specimen and many experimental parameters.

SE generation and emission

SE emission follows an exponential decay law in depth with a typical emission depth about 1 nm; in our calculation Bohmian quantum trajectories are traced up to a length of 1 nm, which is considered appropriate for study of SE imaging. In order to analyze the signal source of atomic resolution SE image, we have recorded energy distributions of generated SEs in inelastic scattering events inside Si bulk (Figs. 6(a) & 6(b)) and of emitted SEs from the specimen surface (Figs. 6(c) & 6(d)). To illustrate the signal contrast, two representative incident locations of a 200 keV electron beam are shown: for the beam incoming along an atom column and landing on the specimen surface of point A shown in Fig. 4(b) (Figs. 6(a) & 6(c)), and for the beam incoming between atom columns and landing on the specimen surface of point B (Figs. 6(b) & 6(d)). In each figure of Fig. 6, we compare the contribution from the directly generated SEs by primary electrons (dotted lines) with that from the cascade SEs

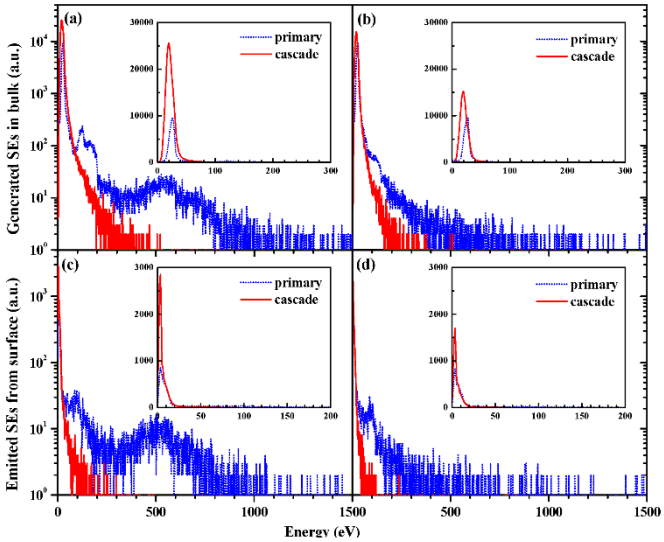

Fig. 6 Simulated energy spectra of SEs for a 200 keV electron incident into Si (110) surface: (a) and (c) for the beam incoming along an atom column and landing on the specimen surface of point A, shown in Fig. 4(b), with the coordinate of (-0.19, 0.27) nm; (b) and (d) for the beam incoming between atom columns and landing on the specimen surface of point B, shown in Fig. 4(b), with the coordinate of (0, 0.27) nm. (a) and (b) SEs at birth where the energy is referenced to bottom of Fermi energy; (c) and (d) SEs emitted from specimen surface where the energy is referenced to vacuum level. Dotted line stands for SEs directly generated by incident electrons in inelastic scattering events and solid line for SEs generated by cascade SEs. The insets show the intensity in linear scale.

in their cascade multiplication process (solid lines). It can be seen that the directly generated SEs by primary electrons present features around 500 and 100 eV, representing the *K*- and *L*-shell excitations respectively, when electrons are incident into the sample along an atom column (Fig. 6(a)). They are clearly the high energy knock-on SEs generated in these inner-shell ionization events by electrons moving close to atoms, while the main peak around 20 eV is certainly due to valence electron excitation. A strong SE peak observed at several eV above vacuum level (Fig. 6(c)), which affords the true image signals detected in a microscope, is seen to be made of valence excitations partially by primary trajectories but dominantly by cascade knock-on SEs. In contrast, when the incident beam lands on the surface and goes into the solid in a far distance from atom columns (Fig. 6(b)) there is no *K*-shell excitation and *L*-shell excitation feature is lower than the case of Fig. 6(a) by more than a half quantity, which can only be observed in the logarithmic plots but not in the insets for the linear plots when comparing Figs. 6(a) and 6(b). It is such a small quantity of high energy SEs produced in inner-shell ionizations that is responsible for the large difference on the quantity of low energy cascade SEs. Therefore, without this extra part of cascade SE multiplication in generation for the beam going into solid between atom columns the final SE emission intensity contributed from cascade multiplication has only about half value in Fig. 6(d) as compared in Fig. 6(c), forming only the image background intensity while those extra cascade SEs generated by high energy knock-on SEs for the beam going into solid along atom columns provide the true image signals. It is therefore clear that the cascade multiplication process plays a key role in the atomic resolution SE imaging and cannot be neglected in any such atomic resolution SE imaging simulation.

Atomic SE imaging of Si crystal

As an application, the present QTMC method is used for study of atomic resolution SE imaging simulation. The breakthrough in SE image resolution challenges the traditional understanding of SE imaging mechanism, which has been considered to be attributed to the delocalized valence electron excitations, either as single electron excitation or through decay of bulk plasmon excitation. The simulation has been performed for a Si (110) crystal in order to compare with experimental observation. The crystal structure is illustrated in Fig. 7(a). A convergent electron probe is normally focused at (110) surface; along the probe incident direction, defined as *z*-axis, it is a double-layer structure. The crystal potential is constructed through Eq. (5) by using Si potential parameters[31]. Fig. 7(b) displays *x*-*y* plane projection of the crystal potential maximum; in the subsequent calculation we have selected a smallest repeatable unit, shown by the red box in Fig. 7(b), as the region of interest (ROI), considering the periodical feature of the crystal specimen. The specimen of 5 nm thickness, which is enough thick for SE signal emission, is considered in calculation. We have considered inner-shell ionizations of Si *K*-, L_1- and $L_{2,3}$-shells, in addition to valence excitations specified by dielectric functional formalism, Eq. (11). The primary electrons and excited electrons will travel in the crystal until they are absorbed, or penetrated from the bottom surface or emitted from the incident surface of the specimen. The SEs emitted from the specimen surface with their energies lower than 50 eV are collected as the signal for SE imaging when primary electron beam scanning over the specimen surface. Our simulation has assumed the following microscope parameters: a probe accelerating voltage of 200 kV, an aperture of 18 mrad, electron-source energy spread of 0.35 eV, a chromatic aberration coefficient of 1.0 mm, a spherical aberration coefficient of 0.0 mm and a defocus of -50 nm.

The SE image simulated by the QTMC method is shown in Fig. 8(a), where a periodic extension based on the selected ROI in Fig. 7(b) is made to give this full image. The atom columns and the double-layer structure of Si (110) crystal, as shown in

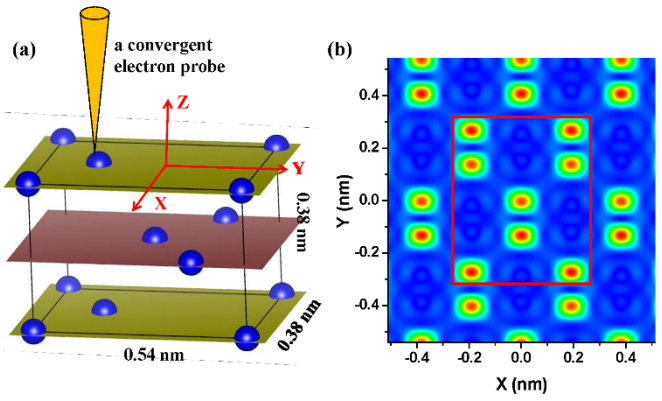

Fig. 7 (a) Illustration of the Si (110) crystal structure. The focused electron probe is normally incident on the specimen surface. (b) The x-y plane projection of the crystal potential maximum; the smallest repeatable unit, shown in the red box, is selected as the ROI in the calculation.

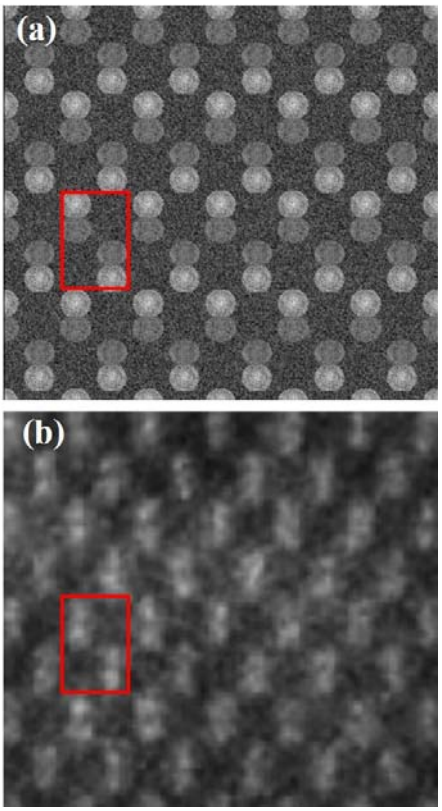

Fig. 8 (a) SE image of Si (110) crystal simulated by the QTMC method; (b) a corresponding experimental SE image[4].

Fig. 8(a), are clearly observed in the simulated SE images. Fig. 8(b) displays a corresponding experimental SE image[4] for a comparison. We can see that the atom positions of the Si dumbbell with a 1.4 Å separation between two projected neighboring Si columns in the simulated image agree well with those in the experimental image. Since the signal-to-noise and contrast in the original experimental image is rather low, we then divide the whole image into identical regions, each containg two dumbbells as shown by the red box in Fig. 8(b), and add the signals in all these regions. After this noise reduction treatment the experimental image is displayed in Fig. 9(a) to compare with the directly simulated image in Fig. 9(b). The atom shape is close to be round in both simulated and experimental images. The weak contrast difference bewteen two atoms in the dumbbell shows a double-layer structure of Si (110) crystal in the simulated image, indicating that the top surface layer should give rise to stronger SE intensity mainly due to the emission process but not to the generation process. However, this contrast is hardly visible in the experimental image most probably because of the noise in the signal detection in experiment. Furthermore, the value of inelastic mean free path λ_{in} of low energy SEs in Eq. (11) also affect theoretical image contrast through the dependence of emission probability on depth.

In the above simulation we have assumed that all the atoms in Si crystal are frozen at the crystalline sites. However, in finite temperature atoms in a crystal vibrate around their equilibrium sites by thermal activation. The thermal vibrations

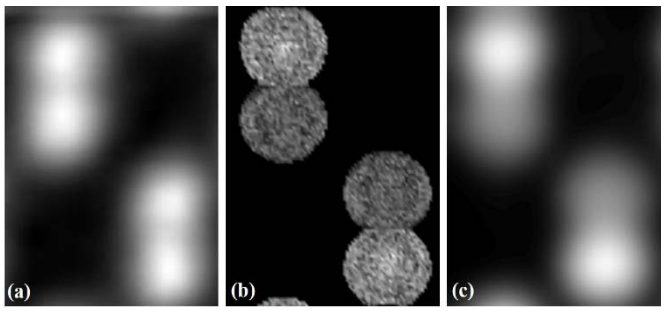

Fig. 9 SE image of Si (110) crystal: (a) averaged image by summing the whole experimental image signals over the periodic region shown by the red box in Fig. 8(b); (b) simulated image by the QTMC method in a periodic region shown by the red box in Fig. 8(a); (c) simulated image by including atomic thermal vibration.

are actually very important for STEM image simulation of nanoparticles[51]. Here, we have taken into account of the atom vibration effect in the SE imaging simulation via a simple classical approach: the probability density function of the atom positions obeys Gaussian distribution $\exp\left(-x^2/2\beta\right)/\sqrt{2\pi\beta}$, and the mean square fluctuation of the distribution β is determined by the entropy $S(x)=S(0)-x^2/2\beta$, which is the expanding of $S(x)$ and terms of up to the second order is retained[52]. The locations of ionization events or the birth sites of high energy knock-on SEs also follow the distribution around equilibrium positions; we can then approximate the simulated SE image by a convolution of image in Fig. 8(a) with a two-dimensional Gaussian function as most those low energy SEs generated in valence excitation contribute only to the image background and are set to intensity zero in Fig. 8(a). The simulated SE image by QTMC after including the atom vibration, shown in Fig. 9(c), presents blurred atom edges and shows more close agreement with experimental image in Fig. 9(a).

Above treatment only approximates atom vibration effect on electron inelastic scattering. A more accurate simulation should also include the effect on electron elastic scattering through electron thermal diffuse scattering (TDS) or electron-phonon interaction. TDS has been included in a Monte Carlo simulation of electron-solid interaction[53] and can be also included into the present QTMC method.

Conclusions

We have presented in this article a new computational method, i.e. the quantum trajectory Monte Carlo (QTMC) simulation, to study the electron interaction with crystalline solid at atomic scale. The method combines Bohmian quantum trajectory method for treating electron elastic scattering and diffraction in a crystal with a conventional Monte Carlo sampling technique of electron inelastic scattering along the trajectory. The quantum trajectories in Cu and Si single crystals are calculated to demonstrate the contraction to propagation along atom columns for a convergent electron probe. The impact parameter dependent cross section for inner-shell ionizations is derived and introduced into the QTMC method to simulate localized high energy knock-on SE generation. The further cascade production of low energy SE signals is simultaed by a

conventional Monte Carlo method. The signal analysis on the simulated energy of SEs has indicated that the high energy knock-on SEs generated in atomic inner-shell ionization by incident electrons travelling along atom columns is the first source of image contrast. We have performed simulation of atomic resolution SE image for Si (110) crystal surface; the simulated image agrees well with the experimental image to show Si dumbbell. However, the simulated weak contrast difference between dumbbell atoms in two different layers still needs further experimental verification. This work has quantitatively revealed that inner-shell ionization produced by high energy incident electron beam is the dominate mechanism for atomic resolution SE imaging by STEM. Our simulation results clearly shows that, the high energy knock-on SEs generated in atomic inner-shell ionization by incident electrons travelling along atom columns should be the first source of image contrast; the further cascade multiplication of low energy SE signal production process plays a role for image contrast, while this cascade process does not destroy the original local information on atomic position. The SE signals are amplified in number but reduced in their energy during the spatial diffusive transportation and emission. In addition, it has been shown that QTMC method is a powerful tool for study of the electron elastic and inelastic scattering in crystalline solid. The optimum experimental condition and/or the minimum beam accelarating voltage required to produce the contrast may also be quantitatively evaluated with this method.

Acknowledgements

This work was supported by the National Natural Science Foundation of China (Nos. 11274288 and 11204289), the National Basic Research Program of China (Nos. 2011CB932801 and 2012CB933702), Ministry of Education of China (No. 20123402110034) and “111” project (No. B07033).

References

1 P.E. Batson, N. Dellby, and O.L. Krivanek, *Nature*, 2002, **418**, 617-620.
2 L.J. Allen, S.D. Findlay, A.R. Lupini, M.P. Oxley, and S.J. Pennycook, *Phys. Rev. Lett.*, 2003, **91**, 105503.
3 Y. Zhu, H. Inada, K. Nakamura, and J. Wall, *Nat. Mater.*, 2009, **8**, 808-812.
4 H. Inada, D. Su, R.F. Egerton, M. Konno, L. Wu, J. Ciston, J. Wall, and Y. Zhu, *Ultramicrosc.*, 2011, **111**, 865-876.
5 S.J. Pennycook, and M. Varela, *J. Electr. Microsc.*, 2011, **60**, S213-S223.
6 Z.J. Ding, and R. Shimizu, *Scanning*, 1996, **18**, 92-113.
7 Z.J. Ding, X.D. Tang, and R. Shimizu, *J. Appl. Phys.*, 2001, **89**, 718-726.
8 S.F. Mao, Y.G. Li, R.G. Zeng, and Z.J. Ding, *J. Appl. Phys.*, 2008, **104**, 114907.
9 H. Kohl, and L. Reimer, Transmission Electron Microscopy: Physics of Image Formation, Springer, New York, 2008.
10 J.M. Cowley, Diffraction Physics, North-Holland, Amsterdam, 1995.
11 Z.L. Wang, Elastic and Inelastic Scattering in Electron Diffraction and Imaging, Springer, New York, 1995.
12 A. Tonomura, J. Endo, T. Matsuda, T. Kawasaki, and H. Ezawa, *Am. J. Phys.*, 1989, **57**, 117-120.
13 L.D. Broglie, *Ann. Phys.*, 1925, **3**, 22-128.
14 D. Bohm, *Phys. Rev.*, 1952, **85**, 166-179.
15 D. Bohm, *Phys. Rev.*, 1952, **85**, 180-193.
16 P.R. Holland, The Quantum Theory of Motion, Cambridge University Press, Cambridge, 1993.
17 C.L. Lopreore, and R.E. Wyatt, *Phys. Rev. Lett.*, 1999, **82**, 5190-5193.
18 C. Philippidis, C. Dewdney, and B.J. Hiley, *Nuov. Cim. B*, 1979, **52**, 15-28.
19 X.Y. Lai, C. Qing-Yu, and M.S. Zhan, *New J. Phys.*, 2009, **11**, 113035.
20 R.G. Zeng, and Z.J. Ding, *J. Surf. Anal.*, 2011, **17**, 198-202.
21 A. Howie, *J. Microsc.*, 1995, **180**, 192-203.
22 R.F. Egerton, Electron Energy-Loss Spectroscopy in the Electron Microscope, Springer, New York, 2011.
23 L. Wu, R.F. Egerton, and Y. Zhu, *Ultramicrosc.*, 2012, **123**, 66-73.
24 H.G. Brown, A.J. D'Alfonso, and L.J. Allen, *Phys. Rev. B*, 2013, **87**, 054102.
25 L. Reimer, Scanning Electron Microscopy: Physics of Image Formation and Microanalysis, Springer, Berlin, 2nd Ed., 1998.
26 X.F. Zhang, *Microsc. Today*, 2011, **19**, 26-29.
27 R.E. Wyatt, Quantum Dynamics with Trajectories, Springer, New York, 2005.
28 M.D. Feit, J.A. Fleck Jr, and A. Steiger, *J. Compu. Phys.*, 1982, **47**, 412-433.
29 E.J. Kirkland, Advanced Computing in Electron Microscopy, 2nd Ed., Springer, New York, 2010.
30 J.C.H. Spence, and J.M. Zuo, Electron Microdiffraction, Springer, New York, 1992.
31 L.M. Peng, *Micron*, 1999, **30**, 625-648.
32 D. Rez, P. Rez and I. Grant, *Acta Cryst. A*, 1994, **50**, 481-497.
33 J.C.H. Spence, and J.M. Cowley, *Optik*, 1978, **50**, 129-142.
34 S.J. Pennycook, and D.E. Jesson, *Phys. Rev. Lett.*, 1990, **64**, 938-941.
35 L. J. Allen and T. W. Josefsson, *Phys. Rev. B*, 1995, **52**, 3184-3198.
36 X. Oriols, *Phys. Rev. L*, 2007, **98**, 066803.
37 A. Alarcon, X. Cartoixa and X. Oriols, *Phys. Status Solidi (c)*, 2010, **7**, 2636-2639.
38 M. Inokuti, *Rev. Mod. Phys.*, 1971, **43**, 297-347.
39 S.J. Pennycook, *Ultramicrosc.*, 1988, **26**, 239-248.
40 R.F. Egerton, *Ultramicrosc.*, 1979, **4**, 169-179.
41 M.C. Walske, *Phys. Rev.*, 1956, **101**, 940-944.
42 B.H. Choi, E. Merzbacher, and G.S. Khandelwal, *Atom. Data Nucl. Data Tables*, 1973, **5**, 291-304.
43 B.H. Choi, *Phys. Rev. A*, 1973, **7**, 2056-2062.
44 B.P. Luo, and E. Zeitler, *J. Electr. Spectrosc. Related Phenom.*, 1991, **57**, 285-295.
45 E. Casnati, A. Tartari, and C. Baraldi, *J. Phys. B*, 1982, **15**, 155-167.
46 D.R. Penn, *Phys. Rev. B*, 1987, **35**, 482-486.
47 E.D. Palik, Handbook of Optical Constants of Solids, Academic Press, San Diego, 3rd Ed., 1998.
48 N. Cao, B. Da, Y. Ming, S.F. Mao, K. Goto, and Z.J. Ding, *Surf. Interface Anal.*, 2015, **47**, 113-119.
49 N.F. Mott, *Proc. Roy. Soc. London A*, 1929, **124**, 425-442.
50 R.G. Zeng, Y. Ming, B. Da, S.F. Mao and Z.J. Ding, (to be submitted).
51 R. Aveyard, R. Ferrando, R.L. Johnston and J. Yuan, *Phys. Rev. Lett.*, 2014, **113**, 075501.
52 L.D. Landau, E.M. Lifshitz. Statistical Physics, Part 1 (3rd ed.), Pergamon, Oxford, 1980.
53 J.S. Villarrubia, A.E. Vladar, B. Ming, R.J. Kline, D.F. Sunday, J.S. Chawla, S. List, *Ultramicrosc.*, 2015, **154**, 15-28.